

Copyright  
by  
David Roger Miller  
2016

The Thesis committee for David Roger Miller

Certifies that this is the approved version of the following thesis:

**Extending the Depth Limit of Multiphoton Microscopy  
for *in vivo* Brain Imaging**

APPROVED BY

SUPERVISING COMMITTEE:

---

Andrew K. Dunn, Supervisor

---

Hsin-Chih "Tim" Yeh

**Extending the Depth Limit of Multiphoton Microscopy  
for *in vivo* Brain Imaging**

by

**David Roger Miller, B.A.**

**Thesis**

Presented to the Faculty of the Graduate School  
of the University of Texas at Austin  
in Partial Fulfillment  
of the Requirements  
for the Degree of

**Master of Science in Engineering**

The University of Texas at Austin

August 2016

Dedicated to my loving parents, Shelley and Marvin.

## Acknowledgments

I wish to thank my advisor Dr. Andrew Dunn for his guidance and insight during my journey into exploring the inner workings of the brain.

Words cannot do justice to express my gratitude to my parents, Shelley and Marvin. Your unconditional love and encouragement has allowed me to dedicate myself to a variety of passions.

I thank my siblings for their unwavering support. Sarah, you are a true inspiration in education reform. I look to you for guidance in ways to fill the education gap. Rubin, thank you for your generosity and chess lessons. Rachel, thank you for your kindness and warmth. Levi, I look forward to what you will accomplish in the next few years.

I am deeply indebted to my dear friend and mentor Joel Weisberg. Your encouragement to pursue my curiosity about the intersection of physics and consciousness has led me down a fascinating road. I thank you for instilling in me a deep curiosity about the world and the tools to chase my dreams.

Lastly, I thank the National Science Foundation, National Institute of Health, and the University of Texas at Austin for funding the projects described in this thesis.

# Extending the Depth Limit of Multiphoton Microscopy for *in vivo* Brain Imaging

by

David Roger Miller, M.S.E.  
The University of Texas at Austin, 2016

Supervisor: Andrew K. Dunn

The benefit of high-resolution imaging provided by optical microscopy has resulted in many discoveries in both biology and neuroscience. Two-photon fluorescence microscopy (2PM) is widely used for *in vivo* brain imaging to visualize cerebral vasculature and neuronal physiology. Conventional 2PM using titanium-doped sapphire oscillators is typically limited to imaging depths less than 600  $\mu\text{m}$  due to their short excitation wavelengths (700 -1,000 nm) and low pulse energy ( $\sim 10$  nJ). The ideal approach for deep imaging is to use both longer wavelengths to reduce the effects of scattering by heterogeneous brain tissue and higher energy pulses such that more photons reach the excitation volume at deeper tissue depths.

I perform high-resolution, non-invasive, *in vivo* deep-tissue imaging of the mouse neocortex using multiphoton microscopy with a high repetition rate optical parametric amplifier (OPA). The OPA outputs 400 nJ pulse energies

and is tunable from 1,100 to 1,400 nm. The tunability of the OPA is an advantage over other high-pulse-energy lasers because the OPA wavelength can be matched to the peak absorption of the target fluorophore, enabling the excitation of numerous different fluorophores. I demonstrate an imaging depth of 1,200  $\mu\text{m}$  in vasculature labeled with Texas Red and 1,160  $\mu\text{m}$  in neurons labeled with tdTomato, and perform line scans as deep as 1200  $\mu\text{m}$  to measure the blood flow speed in a single capillary. I also demonstrate deep-tissue imaging using Indocyanine Green (ICG), which is FDA approved and a promising route to translate multiphoton microscopy to human applications.

# Table of Contents

Acknowledgments	v
Abstract	vi
List of Tables	ix
List of Figures	x
Chapter 1. Introduction	1
Chapter 2. Design, build, and characterize a multiphoton microscope system optimized for deep imaging	4
Chapter 3. <i>In vivo</i> Multiphoton Microscopy Imaging of the Mouse Cortex	16
Chapter 4. What is the Maximum Imaging Depth for Multiphoton Microscopy?	24
Chapter 5. Toward Reaching the Maximum Imaging Depth for Multiphoton Microscopy	28
Chapter 6. Conclusion	33
Bibliography	35

## List of Tables

- 2.1 RMS wavefront aberration (in units of waves) at the objective focus for Design A and B, displayed as Design A / Design B.  
12
  
- 4.1 Imaging parameters used for modeling the maximum imaging depth for titanium-doped sapphire oscillators (Ti:S), regenerative amplifiers (RegA), optical parametric oscillators (OPO), and optical parametric amplifiers (OPA). Note that  $\langle P \rangle$  is the average power at the sample surface.  
25

## List of Figures

2.1	The optical parametric amplifier (OPA) laser system. A Ti:S oscillator seeds a regenerative amplifier. The amplified pulse is converted to a longer wavelength by the OPA. . . . .	6
2.2	OPA temporal and spectral characteristics. <b>(a)</b> Interferometric autocorrelation trace of the OPA pulse after the microscope objective. The measured temporal pulse width was $\tau=119$ femtoseconds. <b>(b)</b> Spectrum of OPA for imaging tdTomato at 1,140 nm, Texas Red at 1,280 nm, and ICG at 1,325 nm. . . . .	8
2.3	Custom-built upright multiphoton microscope. The laser beam is controlled laterally by x-y scan mirrors. The beam is then expanded by 5X by a 40 mm scan lens and 200 mm tube lens. Dichroic mirror 1 (DM1) passes through the laser light to a high numerical aperture objective with low magnification. The sample is placed at the focus of the objective. Fluorescence is dpi-collected back through the objective and directed to the detector arm by DM1. Dichroic mirror 2 (DM2) splits the fluorescence into two channels: red and green. The green channel fluorescence is measured by photomultiplier tube 1 (PMT1) which is a -40 PMT, and the red channel fluorescence is measured by photomultiplier tube 2 (PMT1) which can be either a -40 PMT for shorter emission wavelengths of a -50 PMT for longer emission wavelengths. . . . .	15
3.1	<i>In vivo</i> two-photon microscopy images of vasculature labeled with Texas Red. <b>(a)</b> 3D reconstruction of a 1,200 $\mu\text{m}$ stack of vasculature labeled with Texas Red. <b>(b)</b> x-y intensity projections of stack shown in (a). <b>(c)</b> (top) x-y intensity projection at depth of 1200 $\mu\text{m}$ . A line scan was performed at the highlighted red line. (bottom) Line scan at depth of 1200 $\mu\text{m}$ . All scale bars are 50 $\mu\text{m}$ unless otherwise indicated. . . . .	21
3.2	<i>In vivo</i> two-photon microscopy images of vasculature labeled with ICG. <b>(a)</b> Three-dimensional reconstruction of a 1,000 $\mu\text{m}$ stack. <b>(b)</b> x-y intensity projections of stack shown in (a). All scale bars are 50 $\mu\text{m}$ . . . . .	22

3.3	<i>In vivo</i> two-photon microscopy images of neurons labeled with tdTomato. <b>(a)</b> Three-dimensional reconstruction of a 1,160 $\mu\text{m}$ stack of neurons within a mouse brain. <b>(b)</b> x-y intensity projections from stack shown in (a). All scale bars are 50 $\mu\text{m}$ . . .	23
4.1	Maximum imaging depth for a Ti:S oscillator, regenerative amplifier (RegA), optical parametric oscillator (OPO) and amplifier (OPA). . . . .	26
5.1	Comparison of transmission of current objective and new objective with long-wavelength coatings. . . . .	29
5.2	Logarithmic power dependence plot for common fluorophores. The slope indicates the n-photon excitation. . . . .	31
5.3	The three-photon action cross section for Fluorescein across the OPA excitation wavelengths. . . . .	32

# Chapter 1

## Introduction

Optical imaging offers non-invasive, high-resolution *in vivo* microscopy techniques to observe brain tissue and its surrounding environment. Traditional fluorescence microscopy, including confocal microscopy, using one-photon excitation is limited to imaging the superficial tissue surface due to the scattering of short excitation wavelength light in heterogeneous brain tissue. To overcome depth limitations, nonlinear multiphoton excitation is widely used. Two-photon fluorescence laser-scanning microscopy (2PM), developed in the early 1990's [1], uses an ultrafast laser to cause two-photon excitation of a fluorophore in a confined excitation volume. An image is formed by scanning a focused laser beam across a sample as fluorescence is detected. 2PM requires ultrafast lasers to generate sufficient photon density to cause two-photon excitation. The common laser used for 2PM is a titanium-doped sapphire (Ti:S) oscillator because it reliably outputs mode-locked femtosecond pulses with high average power. Ti:S oscillators typically have a maximum pulse energy of 20 nJ (1.5 W average power at repetition rate of 76 MHz) and temporal pulse widths around 100 fs. Ti:S oscillators provide a tunable excitation wavelength between 700 and 1,000 nm, which covers the peak two-photon absorption of a myriad of common fluorophores thus contributing to the popularity of Ti:S

oscillators. 2PM performed with Ti:S oscillators has been shown to reach a maximum imaging depth of 800  $\mu\text{m}$  in the neocortex [2].

One strategy to extend imaging depth is to regeneratively amplify the output of a Ti:S oscillator to create higher energy pulses on the order of microjoules [3]. Higher energy pulses result in more photons reaching the excitation volume at deeper tissue depths. Theer et al. demonstrated an imaging depth of 1,000  $\mu\text{m}$  using a regeneratively amplified Ti:S oscillator at a center wavelength of 925 nm with a maximum pulse energy of 3  $\mu\text{J}$  (600 mW at repetition rate of 200 kHz) [4]. Another strategy to extend imaging depth is to use optical parametric oscillators with longer excitation wavelength to reduce the effects of scattering by tissue. Kobat et al. demonstrated an imaging depth of 1.6 mm using 1,280 nm excitation light with 1.5 nJ pulse energy (80 MHz repetition rate) [5]. The ideal approach for deep imaging is to use both high-energy pulses and longer excitation wavelengths, in particular excitation wavelengths near 1,300 nm or 1,700 nm at which the attenuation length of mouse cortex is maximized. Horton et al. demonstrated an imaging depth of 1.4 mm with a soliton self-frequency shifted fiber laser at 1,700 nm with a 67 nJ pulse energy (1 MHz repetition rate) [6].

In this thesis, I demonstrate *in vivo* deep-tissue imaging in mouse cortex using an optical parametric amplifier (OPA) that is tunable between 1,100 and 1,400 nm. The tunability of the OPA across a wide spectrum is an advantage over other high-pulse-energy lasers because the OPA wavelength can be matched to the peak absorption of the target fluorophore. I achieve an

imaging depth of 1,200  $\mu\text{m}$  in vasculature labeled with Texas Red, and 1,160  $\mu\text{m}$  in neurons expressing tdTomato. Of particular interest to clinicians, I demonstrate deep-tissue 2PM imaging with ICG. ICG is FDA-approved as a contrast agent for humans (ICG angiography is widespread in ophthalmology for retinal blood vessel imaging) and is a promising route to apply multiphoton microscopy to clinical applications [7, 8].

## Chapter 2

# Design, build, and characterize a multiphoton microscope system optimized for deep imaging

### Design and build laser system

An ultrafast optical parametric amplifier (OPA) has the advantage that it is tunable across a wide spectrum range while maintaining high pulse energy. The spectrum range of the OPA depends on the nonlinear crystal used for parametric amplification. Since longer wavelengths are scattered less in the brain,  $\beta$ -barium borate (BBO) crystals are desirable for multiphoton microscopy to obtain a tunable wavelength range from 1,100 nm to 1,400 nm. Additionally, BBO crystals have a high nonlinearity promoting more efficient parametric amplification, and have small dispersion effects for ultrafast pulses [9].

An OPA requires intense input pulses on the order of a few microjoules to allow efficient conversion to longer wavelengths in the BBO crystal. This is done by regeneratively amplifying a Ti:S oscillator seed. Regenerative amplifiers typically have a maximum repetition rate of 250 kHz, which also limits the OPA to a repetition rate of 250 kHz. A faster repetition rate enables faster imaging speed, or longer pixel dwell times. This is advantageous for deep imaging of vasculature labeled with fluorescent dyes because the time at which the vasculature contains a high concentration of the dye is maximized.

Many dyes will clear quickly which significantly reduces the fluorescent signal and consequently imaging depth. To increase the repetition rate of a standard OPA system, a custom synchronization and delay generator was implemented to control the injection of the Ti:S oscillator seed into the regenerative amplifier. By controlling the injection of the seed pulse with an external clock trigger instead of using a clock derived from the Ti:S oscillator repetition rate, the regenerative amplifier can operate at a repetition rate up to 511 kHz while maintaining pulse energies above 5  $\mu$ J.

During amplification of ultrafast pulses at high repetition rates such as 511 kHz, third-order dispersion becomes an issue. Third-order dispersion is difficult to compensate for in a compressor and causes significant reduction in the efficiency of parametric amplification inside the OPA. In the initial design of the regenerative amplifier, the pulse was stretched during the amplification process by passing through a TeO<sub>2</sub> Q-switch which is highly dispersive. The pulse was then compressed by a holographic grating in a 4-pass configuration after amplification. Using this mechanism of stretching and compressing, I observed that doubling the repetition rate of the regenerative amplifier from 250 kHz to 511 kHz also doubled the output power from 1.5 W to 3 W. Thus, I expected the OPA to follow the same trend; however, I observed little increase in the OPA average power at double the repetition rate. Looking at an autocorrelation trace of the regenerative amplifier pulse, it was obvious that the pulse contained third-order dispersion “wings,” which indicated the pulse was not properly being stretched and compressed. This reduced the photon den-

sity at the interaction site in the OPA BBO crystal and consequently reduced the conversion efficiency of the 800 nm input light to longer wavelengths. To reduce the effects of third-order dispersion, the Ti:S oscillator seed pulse was externally stretched by a grating before entering the regenerative amplifier instead of stretching the pulse during each round-trip of amplification inside the regenerative amplifier. This enabled the use of a non-dispersive Q-switch in the regenerative amplifier that was optimized to handle the bandwidth of the Ti:S oscillator seed, resulting in significantly less third-order dispersion. Additionally, a new grating compressor was installed on a motorized stage which allows the user to minimize third-order dispersion based on the OPA output power.

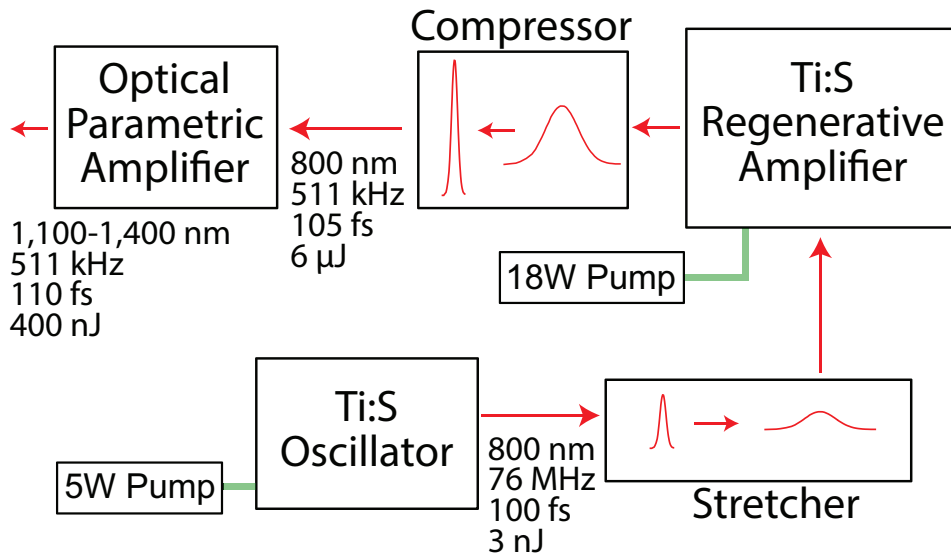


Figure 2.1: The optical parametric amplifier (OPA) laser system. A Ti:S oscillator seeds a regenerative amplifier. The amplified pulse is converted to a longer wavelength by the OPA.

The OPA laser system is shown in Figure 2.1. A  $\lambda=800$  nm mode-locked Ti:S oscillator (Mira 900, Coherent) is externally stretched to seed a regenerative amplifier (RegA 9000, Coherent) that is custom-modified to operate at a tunable repetition rate up to 511 kHz. The seed pulse is amplified to a pulse energy of  $6 \mu\text{J}$  (average power of 3 W at 511 kHz) and then externally compressed. Next, the compressed 800 nm high-energy pulse is converted to a longer wavelength by an OPA (OPA 9800, Coherent) that is tunable between 1,100 and 1,400 nm with a maximum pulse energy of 400 nJ at 511 kHz.

### **Characterize laser characteristics**

To achieve efficient two-photon excitation, laser pulses near 100 fs are desirable. The OPA laser system pulse width is dictated by the Ti:S oscillator seed because its bandwidth determines the lowest possible pulse width of the compressed regenerative amplifier pulse. The regenerative amplifier compressed pulse width significantly affects not only the OPA pulse width but also the OPA output power as discussed above. The Ti:S oscillator is optimized to operate at the minimum angle of deviation for both of its Brewster prisms to achieve the largest bandwidth. I regularly achieve a bandwidth of 12 nm full-width half-maximum (FWHM) in the Ti:S oscillator, equating to a minimum pulse width of roughly 70 fs after the compressor assuming a time-bandwidth product of 0.4 (in between a Gaussian and hyperbolic secant squared pulse shape). I measured the pulse width after the compressor to be 105 fs, which is approaching Fourier-transform limited. As the pulse travels from the OPA to

the microscope, it undergoes some dispersion (primarily in the microscope objective). The OPA temporal pulse width, as measured by *in situ* second order autocorrelation [10], at the output of the microscope objective was measured to be  $\tau=119$  fs, as shown in Fig. 2.2(a).

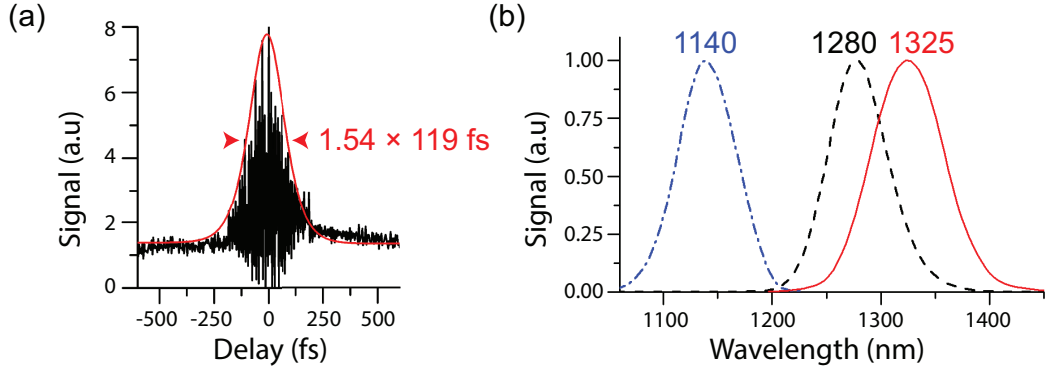


Figure 2.2: OPA temporal and spectral characteristics. (a) Interferometric autocorrelation trace of the OPA pulse after the microscope objective. The measured temporal pulse width was  $\tau=119$  femtoseconds. (b) Spectrum of OPA for imaging tdTomato at 1,140 nm, Texas Red at 1,280 nm, and ICG at 1,325 nm.

Fig. 2.2(b) shows the OPA spectrum used for imaging various fluorophores: tdTomato ( $\lambda=1,140$  nm), Texas Red ( $\lambda=1,280$  nm), and ICG ( $\lambda=1,325$  nm). The OPA can consistently output an average power above 150 mW for the tuning range from 1,140 nm to 1,330 nm, and can operate down to 1,100 nm and up to 1,400 nm with the average power falling off to approximately 50 mW. The OPA bandwidth is about 70 nm FWHM, indicating that the OPA pulse is not Fourier-transform limited and thus could be further compressed. Ideally, the OPA pulse would be pre-chirped to achieve the minimum pulse width at the output of the microscope objective. Pre-chirping

means compensating for the positive dispersion imparted by the microscope optics by applying negative dispersion to the pulse before it enters the microscope. I have opted not to compress the OPA pulse because the maximum grating efficiency is only 70%. Since the maximum imaging depth is proportional to the log of the excitation power whereas its proportional to the log of the square root of the pulse width, it seems advantageous to opt for more power instead of shorter pulse widths. However, future improvements in the OPA power may cause the OPA to approach the safe threshold power limit in which the excitation power would have to be reduced anyways, so it would be worth losing 30% of the light for a shorter pulse.

### **Improve microscope optics for longer excitation wavelength light**

Before my tenure in the Dunn lab at UT Austin, a custom upright two-photon microscope was built as described in [11]. The microscope optics were designed for Ti:S oscillator excitation wavelengths between 800 and 900 nm, and the microscope was not optimized for large scan angles which resulted in vignetting when trying to image more than a 400  $\mu\text{m}$  by 400  $\mu\text{m}$  area. In preparation for deep-tissue imaging with the OPA, I modified the microscope for longer excitation wavelengths and optimized the scanning optics.

The previous microscope used a  $f=20$  mm bi-convex scan lens (NIR-coated) and  $f=125$  mm bi-convex tube lens (NIR-coated) to expand the beam by 6X such that the incoming 3 mm laser beam would fill the 18 mm back aperture of the microscope objective. To avoid vignetting, the scan lens was

designed to be placed a focal length away from the scanning galvanometer mirrors such that there is no lateral displacement of the expanded beam on the back aperture of the objective. Due to the large beam size and consequently large galvanometer mirrors (5 mm), vignetting occurred when scanning over large areas because the optical path varied by about 4 mm between the galvanometer mirrors and scan lens, resulting in alignment error up to 20%. In conclusion, the focal length of the scan lens (20 mm) was not sufficiently larger than the change in the optical path for large scan angles.

To remedy the problem, I investigated using a longer focal length scan lens. The previous microscope expanded the beam by 6X, however I found that the beam had diverged to a diameter of 4 mm when it reached the galvanometer mirrors, thus only a 5X expansion was needed to back fill the 18 mm aperture. In choosing the focal length of the scan and tube lens, the microscope casing posed a restriction to the amount that the galvanometer mirrors could be raised to accommodate longer focal lengths. I found that the maximum focal lengths allowed to expand the beam 5X while fitting within the microscope casing was a  $f=40$  mm scan lens and  $f=200$  mm tube lens.

A second design consideration was avoiding lenses that contain significant amount of metal dopant ions, namely short focal length lenses and doublets, which undergo luminescence at near infrared wavelengths [12]. To achieve high indices of refraction, rare-earth elements are often added to the optical glass; while this enables lenses to be made thinner and thus reduce spherical aberration, the dopant ions undergo upconversion and luminesce in

wavelength regions that interfere with the detection of intended fluorescent signal [12]. The upconversion process involves real energy states, not virtual states as in two-photon excitation. Thus, the likelihood of the unwanted luminescence increases with the amount of spatial interaction of the laser pulse and glass, as opposed to locations of high peak pulse energy due to focusing of the beam. Therefore, luminescence was more likely occurring in the tube lens rather than the scan lens since the beam is about 20 mm when it reaches the tube lens compared to 4 mm when it reaches the scan lens. I chose to implement a Plössl eyepiece design for the scan lens which uses identical achromatic doublets placed symmetrically around a minute air gap. For multiphoton microscopes, a Plössl design outperforms a single achromatic doublet in terms of reducing aberrations [13]. To investigate whether to use an achromatic doublet or plano-convex lens for the tube lens, I modeled each design in the ray-tracing program Zemax. Design A used a  $f=40$  mm Plössl scan lens and a  $f=200$  mm achromatic doublet tube lens, while Design B used a  $f=40$  mm Plössl scan lens and a  $f=200$  mm plano-convex tube lens. Although one would expect better performance with an achromatic doublet for the tube lens (Design A), the plano-convex lens uses significantly less dopants and thus would alleviate concerns about unwanted luminescence generated in the lens.

I modeled the scan angle for three different configurations: on-axis,  $3^\circ$  off-axis in the x-direction (which equates to a 2 mm by 2 mm scan area for the 20X objective), and  $3^\circ$  off-axis in the y-direction. I used the Olympus XLUMPLFLN 20X 0.95 NA microscope objective in the model to determine

the wavefront aberration at the focus of the objective using a custom merit function. While I wanted to optimize the multiphoton microscope for the OPA excitation wavelengths between 1,100 and 1,400 nm, the microscope is also used for imaging at 800 nm with a Ti:S oscillator and near 1,050 nm with a fiber laser. For this reason, I chose to use Thorlabs' B-coating for the optics, which has greater than 99.5% transmission from 700 to 1080 nm and greater than 95% transmission out to 1,400 nm. While the Thorlabs C-coating would be more ideal for the OPA wavelengths as it has a transmission above 99.5% from 1,100 to 1,400 nm, the C-coating performs poorly at 800 nm (85% transmission). Table 2.1 shows the RMS wavefront aberration at the focus of the objective for Design A and B for 800, 1,000, and 1,300 nm over the three aforementioned scan angles. Note that a wavefront error RMS of 0.072 waves or less is considered diffraction-limited [13].

Table 2.1: RMS wavefront aberration (in units of waves) at the objective focus for Design A and B, displayed as Design A / Design B.

$\lambda$ (nm)	<b>Design A / Design B</b>		
	On-Axis	3° in X	3° in Y
800	.087/.198	.076/.191	.162/.295
1,000	.031/.031	.031/.129	.085/.073
1,300	.068/.200	.012/.299	.089/.281

The results of Table 2.1 indicate the difficulty in optimizing scanning optics over a large wavelength range from 800 nm to 1,300 nm for large scan angles as neither design achieves diffraction-limited resolution for all wavelengths over all scan angles. The best wavelength for both designs is 1,000 nm, which

is likely a product of it being in the middle of the three selected wavelengths and the choice of Thorlabs B optical coatings, which are optimized for wavelengths from 700 to 1,100 nm. Design A clearly out performs Design B as only a few configurations in Design A are far from diffraction-limited, whereas just 2 of 9 configurations are diffraction-limited for Design B. However, Design B does not lag too far behind Design A. I chose Design B to ensure luminescence would not disrupt the collection of intended fluorescent signal.

Another necessary improvement was the collection efficiency of the fluorescent light. The previous microscope used a 740dccxr dichroic (Chroma) to reflect the fluorescent light toward the detector while letting the excitation light pass through. The 740dccxr dichroic has a transmission of greater than 98% from 750 to 850 nm, making it ideal for Ti:S oscillator wavelengths. However, the 740dcxxr has less than 1% transmission above 1275 nm. The 740dcxxr dichroic was thus replaced with a 775 nm edge multiphoton dichroic (Semrock) that has greater than 96% transmission from 780 nm to 1600 nm, thus allowing both the OPA excitation wavelengths to pass through as well as the Ti:S oscillator (800 nm) and fiber laser (1,050 nm).

For some deep imaging experiments, fluorescent dyes that emit fluorescence longer than 780 nm are desirable. For example, Indocyanine Green (ICG) emits near 830 nm. Dyes with red-shifted emission spectrum such as ICG have the benefit that the fluorescence is less scattered by heterogenous brain tissue. For these experiments, a dichroic that would pass the OPA wavelengths but reflect fluorescence below about 850 nm is needed. I opted

for a 875 nm edge multiphoton dichroic (Semrock) that has greater than 96% transmission from 900 nm to 1500 nm. Additionally, a detector that was sensitive to fluorescence near 800 nm was needed. The previous microscope used photomultiplier tube (PMT) detectors with peak sensitivity at  $\lambda=580$  nm (H10770PB-40, Hamamatsu Photonics) in both detection channels. While the -40 PMTs are adequate for detecting fluorescence in the visible range, which is typical for fluorophores excited by Ti:S oscillators, they are weakly sensitive to fluorescence near 800 nm. Thus, the option of using a PMT with peak sensitivity at  $\lambda=800$  nm (H10770PB-50, Hamamatsu Photonics) was installed.

Figure 2.3 shows the microscope design. The laser is scanned with an xy-galvanometer mirror pair (Cambridge Technologies, 6125H), and then expanded via a Plössl scan lens (40 mm) and tube lens (200 mm) to fill the back aperture of the microscope objective (XLUMPLFLN 20X 0.95 NA, Olympus). Fluorescence is epi-collected and directed to the PMT detectors by dichroic mirror DM1 and split into two channels by dichroic mirror DM2. The collected PMT signal is synchronized with the regenerative amplifier. Custom software controls the image acquisition.

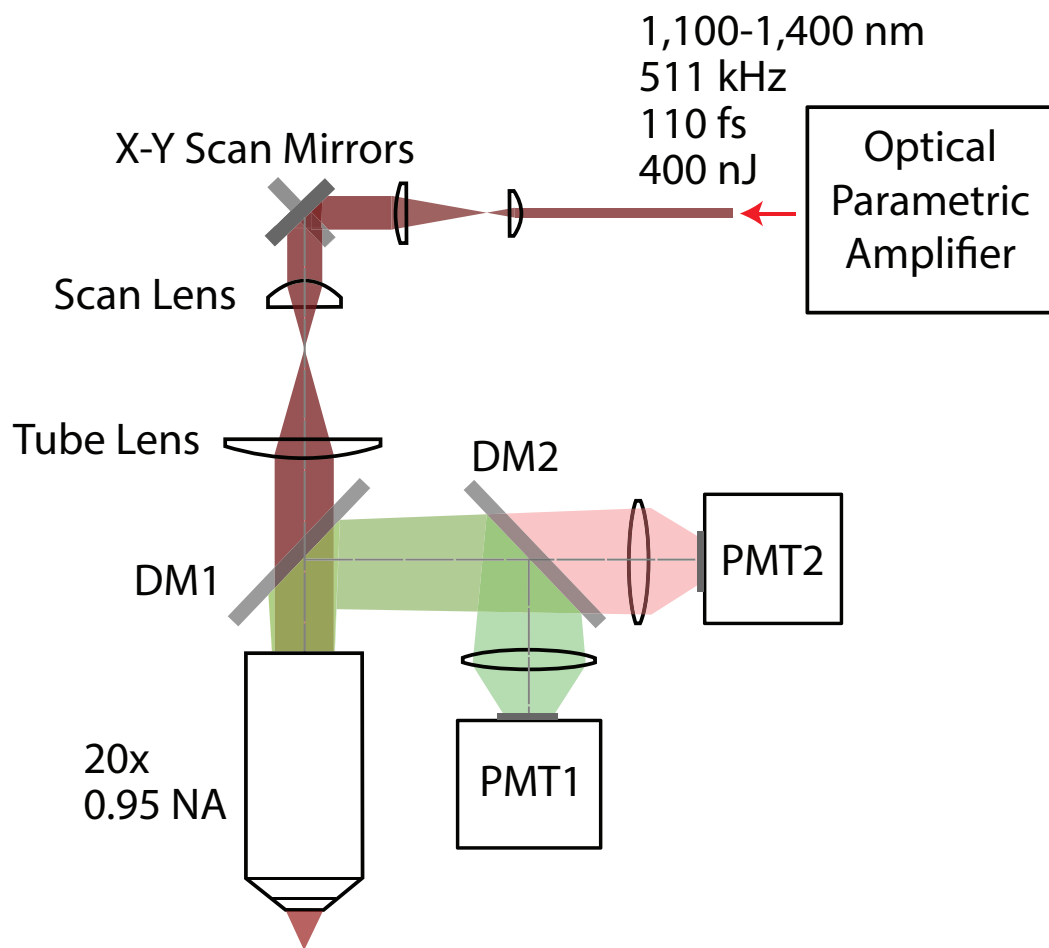


Figure 2.3: Custom-built upright multiphoton microscope. The laser beam is controlled laterally by x-y scan mirrors. The beam is then expanded by 5X by a 40 mm scan lens and 200 mm tube lens. Dichroic mirror 1 (DM1) passes through the laser light to a high numerical aperture objective with low magnification. The sample is placed at the focus of the objective. Fluorescence is dpi-collected back through the objective and directed to the detector arm by DM1. Dichroic mirror 2 (DM2) splits the fluorecence into two channels: red and green. The green channel fluorecence is measured by photomultiplier tube 1 (PMT1) which is a -40 PMT, and the red channel fluorecence is measured by photomultiplier tube 2 (PMT1) which can be either a -40 PMT for shorter emission wavelengths or a -50 PMT for longer emission wavelengths.

## Chapter 3

### ***In vivo* Multiphoton Microscopy Imaging of the Mouse Cortex**

To demonstrate the ability of the OPA laser system to image deep tissue, I performed *in vivo* multiphoton microscopy with three different fluorophores: Texas Red and ICG to label vasculature, and tdTomato to label neurons. The OPA laser system has the ability to image beyond 1 mm in all three fluorophores, extending the traditional depth limit in 2PM.

Two-photon microscopy images were separately acquired in different mice for the three fluorophores - Texas Red, ICG, and tdTomato. Appropriate emission filters were placed in front of each PMT. For imaging Texas Red, a 750 nm short pass (FF01-750/SP-25, Semrock) and 610 nm band pass (HQ/610/75M, Chroma) were used. For imaging ICG, a 594 nm long pass (BLP01-594R-25, Semrock) and 830 nm bandpass (RT-830, Edmund Optics) were used. For imaging tdTomato, a 750 nm short pass and 609 nm band pass (FF01-609/181-25, Semrock) were used. For imaging Texas Red and tdTomato, I used the 775 nm edge dichroic for DM1 and -40 PMT; for imaging ICG, I used the 875 nm edge dichroic for DM1 and -50 PMT. Heavy water was used as the immersion medium to reduce absorption of the OPA excitation

light. Each pixel corresponds to two pulses from the OPA. All frames are 512 by 512 pixels and all stacks are in 5  $\mu\text{m}$  depth increments. The laser power was adjusted throughout each stack with a half-wave plate and polarizing beam splitter to ensure sample damage did not occur [14]. I observed no damage to vasculature or neurons and was able to image the mice chronically. Rendering of three-dimensional (3D) stacks was performed with visualization software (Aviso standard, VSG). The yellow dotted line in each 3D stack signifies the reference plane for which all frames below were normalized; all frames above were normalized individually.

All animal procedures were approved by The University of Texas at Austin Institutional Animal Care and Use Committee. Cranial window implants were prepared in C57 mice and left the dura intact as described in [15]. Mice were anesthetized with isoflurane throughout surgery and imaging. Body temperature was maintained at 37.5° Celsius and 0.1 mL subcutaneous injections of 5% (w/v) glucose in physiological saline were applied every 2 hours. For imaging Texas Red and ICG, a retro-oribital injection of the fluorescent dye was performed to label blood plasma in the vasculature. For imaging tdTomato, neurons were labeled by cortical injection of adeno-associated viral vectors carrying a tdTomato plasmid. Imaging sessions were performed a week following the delivery of the viral vectors.

Fig. 3.1(a) demonstrates an imaging depth of 1,200  $\mu\text{m}$  for vasculature labeled with Texas Red. The excitation power was increased to maintain similar signal levels down to 800  $\mu\text{m}$ , at which point full power was reached

equating to 34 mW at the sample surface (transmission of the objective at 1,280 nm is 32%). In Fig. 3.1(b), individual blood vessels can be seen with high contrast beyond 800  $\mu\text{m}$ , and still resolved beyond 1,100  $\mu\text{m}$ . During the acquisition of the 3D stack, I averaged for 5 frames from 0 to 500  $\mu\text{m}$ , 10 frames from 500 to 700  $\mu\text{m}$ , and 30 frames from 700 to 1,200  $\mu\text{m}$ . Fig. 3.1(c) demonstrates the system's ability to perform line scan in individual capillaries at an imaging depth of 1,200  $\mu\text{m}$ . During a line scan, the laser is scanned back and forth over a blood vessel, which causes red blood cells flowing through the vessel to appear as streaks. The streaks are analyzed to reveal the blood flow velocity in the vessel. In Fig. 3.1(c), the highlighted red line (top) indicates the position of the line scans (bottom). To the best of my knowledge, this is the deepest line scan performed *in vivo* to date. The blood flow speed was measured to be  $1.1 \pm 0.1$  mm/s.

Figure 3.2(a) shows a 3D rendering of vasculature labeled with ICG with an imaging depth of 1,000  $\mu\text{m}$ . Blood vessels can be resolved throughout the stack. Excitation power was increased to maintain similar signal levels down to 750  $\mu\text{m}$  at which point full power was reached equating to 20 mW at the sample surface (the transmission of the objective at 1,325 nm is 28%). ICG is FDA approved for human use and is commonly used for ICG angiography in ophthalmology. Its far-red fluorescence emission near 830 nm makes it an ideal candidate for translating deep-tissue multiphoton microscopy to clinical applications. One draw back to ICG for deep imaging is its quick clearance time. I found that ICG was significantly cleared from cerebral vasculature after

30 minutes, which caused a heterogeneous distribution of fluorescence signal throughout the 3D reconstruction in Fig. 3.2(a). After the first injection of ICG, it took approximately 15 minutes to select a region of the brain without large surface vessels, which can cause significant out-of-focus fluorescence at deep imaging depths. Thus, the ICG dye had started to clear by the time the first 400  $\mu\text{m}$  were imaged, which is why only large vessels are visible in the first 400  $\mu\text{m}$ . At 400  $\mu\text{m}$ , more ICG was injected and then imaging began immediately afterwards; thus, there is a clear increase in signal starting at 400  $\mu\text{m}$ . Only two injections of ICG were performed to avoid injecting more than 20% of the mouse's total blood volume, which limited the number of frames over which I could average such that the stack could be acquired before the dye cleared. I performed a 5 frame average from 0 to 700  $\mu\text{m}$  below the surface, 8 frame average from 700 to 800  $\mu\text{m}$ , 10 frame average from 800 to 900  $\mu\text{m}$ , and 12 frame average from 900 to 1,000  $\mu\text{m}$ .

Figure 3.3(a) demonstrates an imaging depth of 1,160  $\mu\text{m}$  in neurons expressing tdTomato. Excitation power was increased to maintain similar signal levels down to 850  $\mu\text{m}$  at which point full power was reached equating to 40 mW at the sample surface (the transmission of the objective at 1,140 nm is 52%). The delivery of tdTomato causes roughly a 200  $\mu\text{m}$  by 200  $\mu\text{m}$  transversal area of expression after a week following injection. The expression is strongest in the center of the transversal area, which is why the 3D reconstruction in Fig. 3.3(a) appears saturated in the transversal center. Individual neurons and their dendrites are visible throughout the stack, as shown in the

x-y intensity projections in Fig. 3.3(b). Fluorescent proteins like tdTomato have the advantage that they are not cleared, and they are typically much brighter than fluorescent dyes. For the 3D reconstruction of neurons labeled with tdTomato in Figure 3.3(a), I averaged for 5 frames from 0 to 800  $\mu\text{m}$ , 8 frames from 800 to 900  $\mu\text{m}$ , 20 frames from 900 to 1,000  $\mu\text{m}$ , and 25 frames from 1,000 to 1,1600  $\mu\text{m}$ .

In conclusion, the benefits of the OPA - high pulse energy and long excitation wavelengths at which scattering in the mouse brain is minimized - enable it to extend the traditional imaging depth of 2PM. I have demonstrated that the OPA system can reach an imaging depth of 1,200  $\mu\text{m}$  in vasculature and 1,160  $\mu\text{m}$  in neurons. Next, I will examine the expected maximum imaging depth of the OPA system.

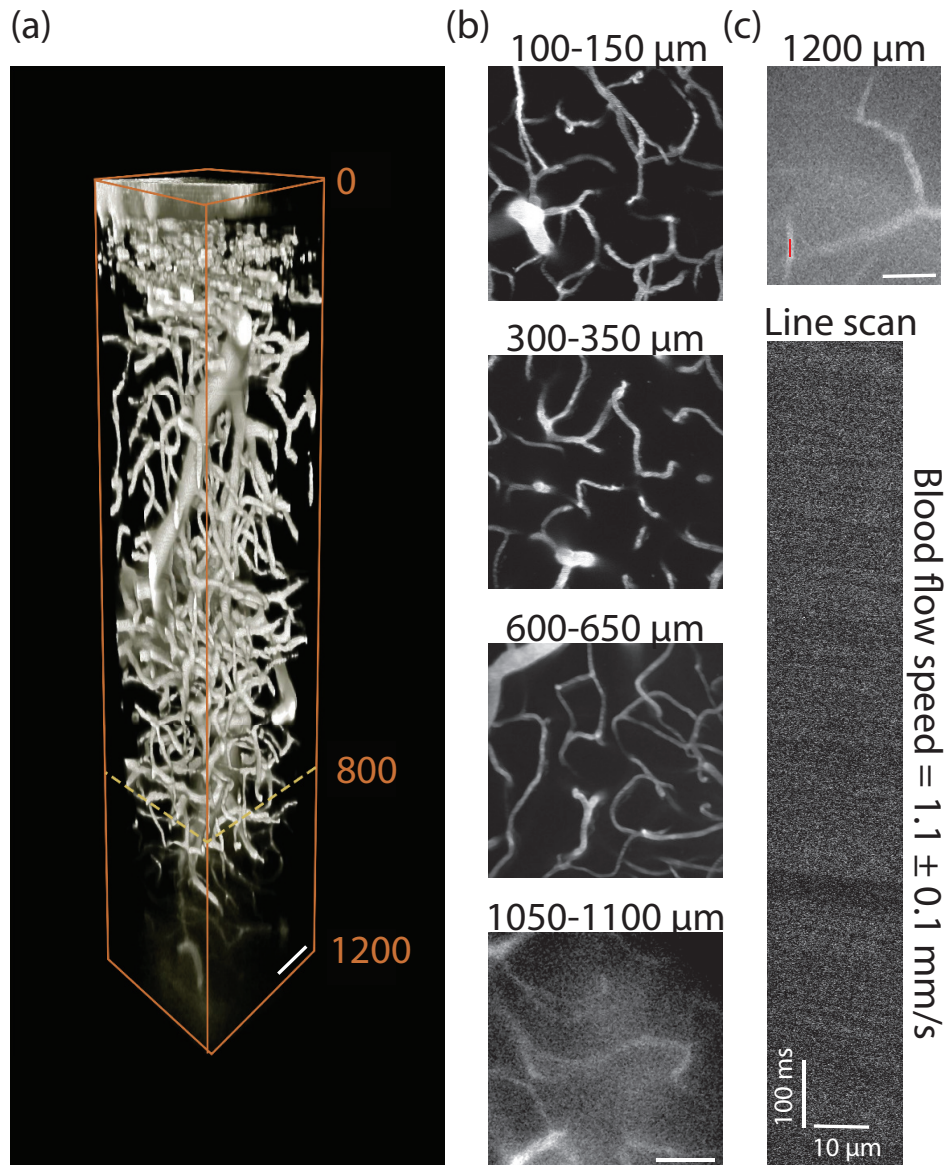


Figure 3.1: *In vivo* two-photon microscopy images of vasculature labeled with Texas Red. (a) 3D reconstruction of a 1,200  $\mu\text{m}$  stack of vasculature labeled with Texas Red. (b) x-y intensity projections of stack shown in (a). (c) (top) x-y intensity projection at depth of 1200  $\mu\text{m}$ . A line scan was performed at the highlighted red line. (bottom) Line scan at depth of 1200  $\mu\text{m}$ . All scale bars are 50  $\mu\text{m}$  unless otherwise indicated.

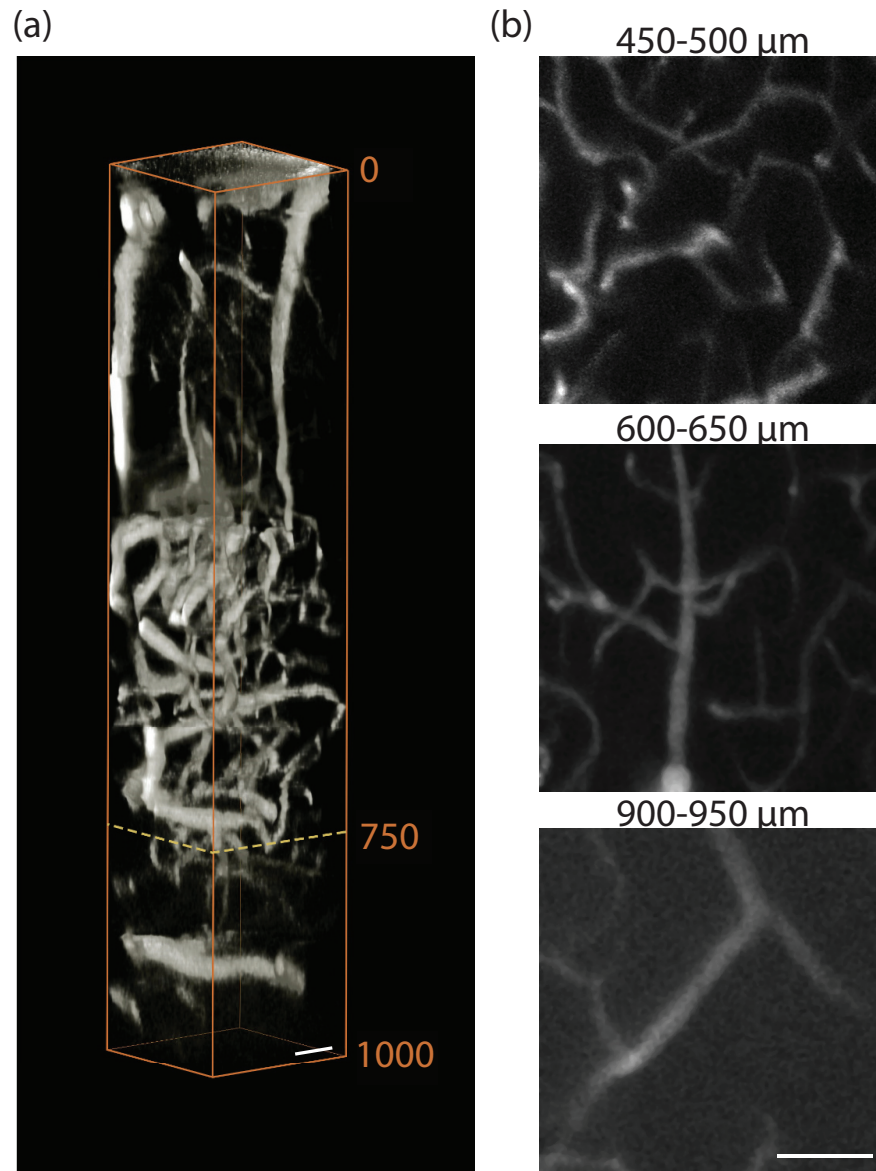


Figure 3.2: *In vivo* two-photon microscopy images of vasculature labeled with ICG. (a) Three-dimensional reconstruction of a 1,000  $\mu\text{m}$  stack. (b) x-y intensity projections of stack shown in (a). All scale bars are 50  $\mu\text{m}$ .

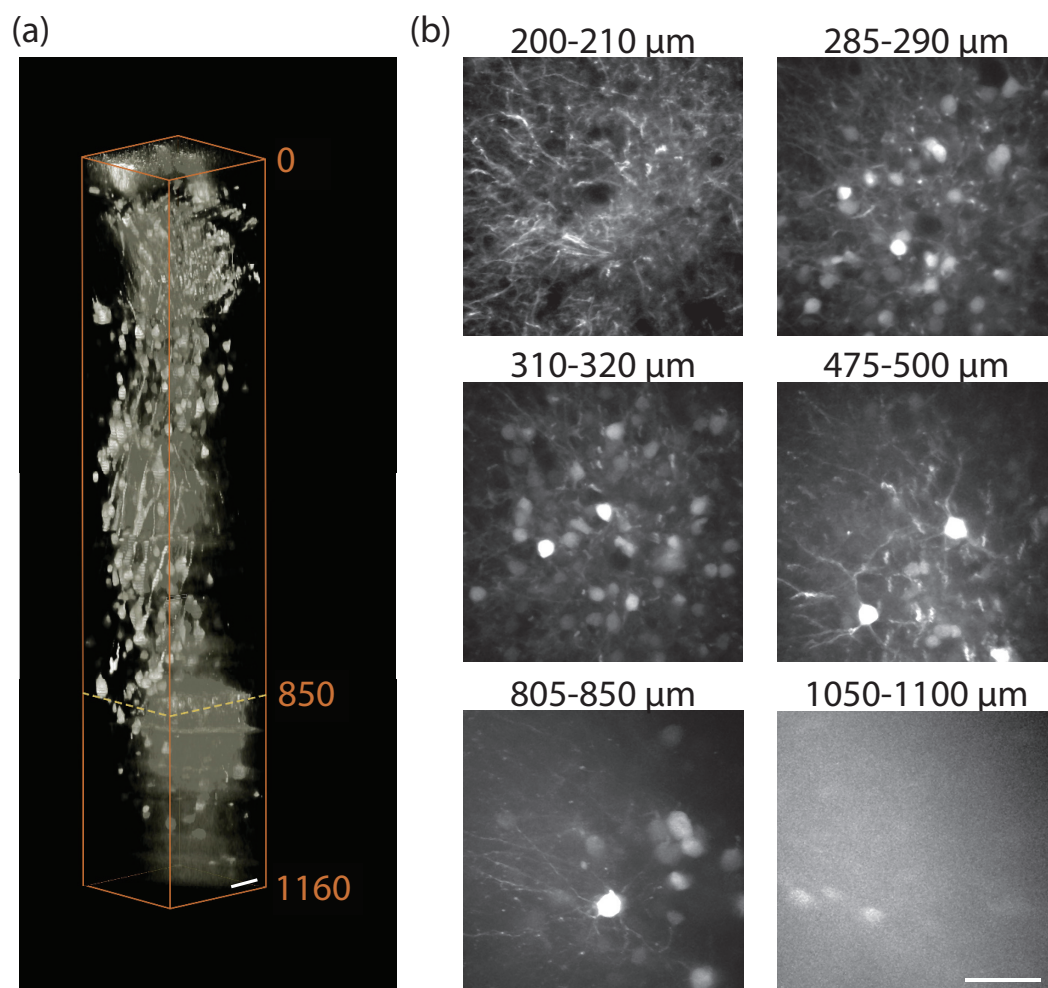


Figure 3.3: *In vivo* two-photon microscopy images of neurons labeled with td-Tomato. (a) Three-dimensional reconstruction of a 1,160  $\mu\text{m}$  stack of neurons within a mouse brain. (b) x-y intensity projections from stack shown in (a). All scale bars are 50  $\mu\text{m}$ .

## Chapter 4

### What is the Maximum Imaging Depth for Multiphoton Microscopy?

There are two competing theories to determine the maximum imaging depth,  $z_{\max}$ , for 2PM. The first defines the maximum imaging depth when the signal to background ratio (S/B), defined as

$$\frac{S}{B} = \frac{2\pi(NA)^2}{\lambda n l_s} z^2 \exp(-2z/l_s), \quad (4.1)$$

becomes unity [4]. Here,  $NA$  is the numerical aperture of the objective,  $\lambda$  is the excitation wavelength,  $n$  is the index of refraction of the medium, and  $l_s$  is the scattering length of mouse brain cortex. The underlying assumption for this theory is that out-of-focus fluorescence generated at the surface due to the increasing beam cross section at the surface eventually overpowers the fluorescent signal generated at the focus. While this condition is certainly true if there are large surface blood vessels above the focus, the situation can be avoided by finding brain regions with no large surface vessels.

The second theory bases the maximum imaging depth on the signal-to-noise ratio, not the signal-to-background ratio. The maximum imaging depth is defined as

$$z_{\max} = l_s \ln \left[ \sqrt{\frac{\sigma_2}{n_{\min} \tau f} \frac{\pi(NA)^2}{hc\lambda} \langle P \rangle} \right], \quad (4.2)$$

where  $\sigma_2$  is the two-photon absorption cross section,  $n_{\min}$  is the minimum number of photon pairs absorbed per fluorophore per unit time,  $\tau$  is the pulse width,  $f$  is the repetition rate of the laser,  $h$  is Planck's constant,  $c$  is the speed of light in vacuum, and  $\langle P \rangle$  is the average power of the laser. This equation seems more accurate as it accounts for the brightness of the target fluorophore  $\sigma_2$  as well as the laser characteristics  $f$  and  $\tau$ . The imaging results presented in Chapter 3 support this theory. To evaluate whether Equation 4.2 agrees with experimental results, I evaluated  $z_{\max}$  for Ti:S oscillators, regenerative amplifiers, optical parametric oscillators (OPO), and optical parametric amplifiers for typical laser parameters, shown in Table 4.1.

Table 4.1: Imaging parameters used for modeling the maximum imaging depth for titanium-doped sapphire oscillators (Ti:S), regenerative amplifiers (RegA), optical parametric oscillators (OPO), and optical parametric amplifiers (OPA). Note that  $\langle P \rangle$  is the average power at the sample surface.

	Ti:S	RegA	OPO	OPA
$f$ (MHz)	76	.250	80	.500
$\tau$ (fs)	100	100	140	120
$\langle P \rangle$ (mW)	560	45	120	30
NA	1.0	1.0	1.0	1.0
$\sigma_2$ (GM)	50	50	50	50

Figure 4.1 shows the maximum imaging depth for each laser assuming a  $NA$  of 1.0, two-photon cross section of  $\sigma_2=50$  GM, and  $n_{\min}$  such that

$$\frac{n_{\min}}{f} \cdot N_p \cdot N_f = 50 , \quad (4.3)$$

where  $N_p$  is the number of pulses per pixel and  $N_f$  is the number of frames averaged at the maximum imaging depth.

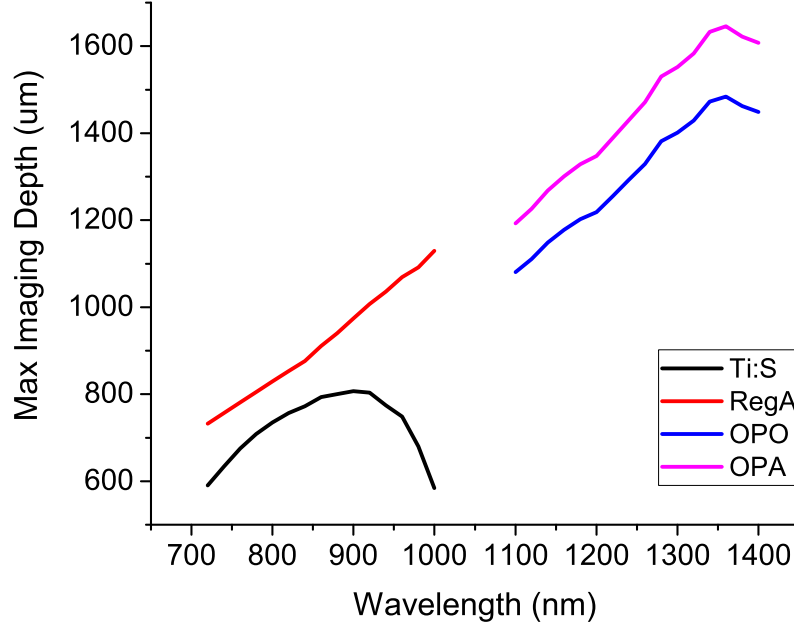


Figure 4.1: Maximum imaging depth for a Ti:S oscillator, regenerative amplifier (RegA), optical parametric oscillator (OPO) and amplifier (OPA).

Figure 4.1 is in general agreement with experimental results. The predicted maximum imaging depth for a: Ti:S oscillator is around  $800 \mu\text{m}$  as found in [2], regenerative amplifier is around  $1,000 \mu\text{m}$  as found in [4], and OPO is around  $1,500 \mu\text{m}$  as found in [5]. The maximum imaging depth of the OPA is about  $150 \mu\text{m}$  more than the OPO at each wavelength, a result of higher energy pulses penetrating deeper into tissue. The imaging results displayed in Chapter 3 demonstrate an imaging depth of  $1,200 \mu\text{m}$ , which is about  $400 \mu\text{m}$  from the theoretical limit (assuming a 50 GM fluorophore). The reason the presented imaging results in Chapter 3 are not near the maximum

imaging depth is due to the attenuation of the OPA power as it travels from the laser to the sample surface. I will discuss methods to improve upon this in the next chapter.

Figure 4.1 arbitrarily uses 50 GM as the fluorophore brightness, however, it would be useful to characterize the imaging depth for each individual fluorophore based on its wavelength-dependent two-photon action cross section. A complete characterization of the brightness combined with a model predicting maximum imaging depth will help to identify the optimal wavelengths for deep imaging. Another parameter to consider is the wavelength-dependent output power of the OPA (only the Ti:S oscillator power was modeled as wavelength-dependent in Figure 4.1). Future work should incorporate the wavelength dependence of both absorption cross sections and laser power to better predict the maximum imaging depth of a laser system and its target fluorophore.

## Chapter 5

# Toward Reaching the Maximum Imaging Depth for Multiphoton Microscopy

### Increasing the OPA power at the sample surface

The power reaching the sample is currently the limiting factor in imaging depth. To achieve higher power at the sample, two methods will be implemented. First, the regenerative amplifier will be increased to a repetition rate of 750 kHz while maintaining the same pulse energy, which should increase the OPA output power by 50%. Second, a microscope objective with coatings optimized for the OPA excitation wavelengths will be used, increasing the transmission from 30% to greater than 70%. The improvement in transmission between the current objective (XLUMPLFLN 20X W) and new objective (XLPLN 25X WMP2) is shown in Figure 5.1. Additionally, the XLPLN 25X WMP2 microscope objective has a working-distance of 4 mm, enabling the possibility for imaging beyond 2 mm, which is the working distance of the XLUMPLFLN 20X W objective.

### Optimizing the target fluorophore and excitation wavelength

To further extend imaging depth, it is crucial to know what fluorophores are brightest and at what excitation wavelengths. The two-photon action

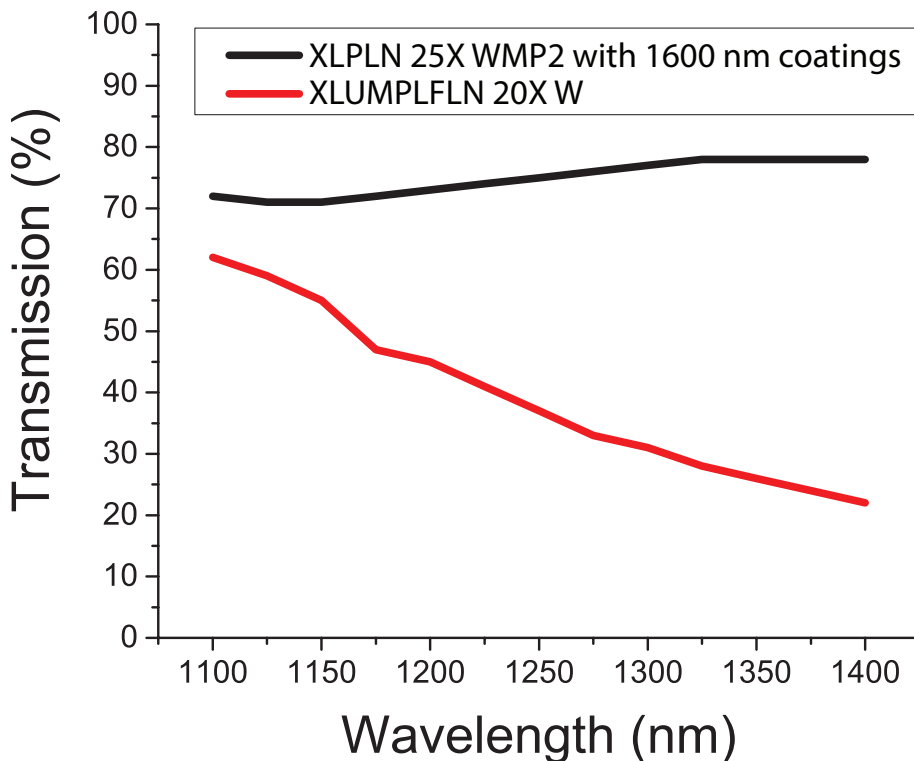


Figure 5.1: Comparison of transmission of current objective and new objective with long-wavelength coatings.

cross section is a measure of brightness for a fluorophore at a particular wavelength. The two-photon action cross sections for most common fluorophores have been characterized for the Ti:S oscillator wavelength range from 700 to 1,000 nm [16–19], including for fluorescent proteins [20]. This has led to a rise in popularity of 2PM with Ti:S oscillators because users can quickly identify the ideal fluorophore for their application. Unfortunately, there is little literature characterizing the two- and three-photon cross sections of fluorophores for the OPA wavelength range from 1,100 to 1,400 nm. In fact, I am aware of

just two papers in the literature that report cross section values between 1,100 and 1,400 nm [21, 22], even though there are increasingly more papers demonstrating *in vivo* deep-tissue imaging at longer wavelengths [5, 6, 15]. There is thus a strong need to characterize the two- and three-photon cross sections of common fluorophores at longer wavelengths.

I performed preliminary work identifying multiple common fluorophores that undergo two- or three-photon excitation at longer wavelengths. To determine whether the fluorescence from each fluorophore was the result of two-photon excitation (2PE) or three-photon excitation (3PE), I measured the dependence of the fluorescence on excitation power in a cuvette. The slope of the logarithmic plot indicates whether the generated fluorescence is due to 2PE or 3PE. Figure 5.2 shows the power dependence for the fluorescent dyes: Fluorescein, Rhodamine B, Ruthenium, Texas Red, and ICG, and the fluorescent protein: yellow fluorescent protein (YFP). The power dependence was determined by exciting Fluorescein, Ruthenium, and Rhodamine B at  $\lambda=1243$  nm, Texas Red at  $\lambda=1296$  nm, YFP at  $\lambda=1330$  nm, and ICG at  $\lambda=1315$  nm. A slope near 3.0 for Fluorescein, Rhodamine B, Ruthenium, and YFP indicate they undergo 3PE. A slope near 2.0 for ICG indicates it undergoes 2PE. Near an excitation wavelength of 1,280 nm, Texas Red undergoes 2PE at low excitation powers; however, Texas Red undergoes both 2PE and 3PE at higher excitation powers, indicated by a slope of 2.53. For the imaging experiments with Texas Red shown in Fig. 3.1, we expect that the excitation power at the samples focus is in the 2PE regime.

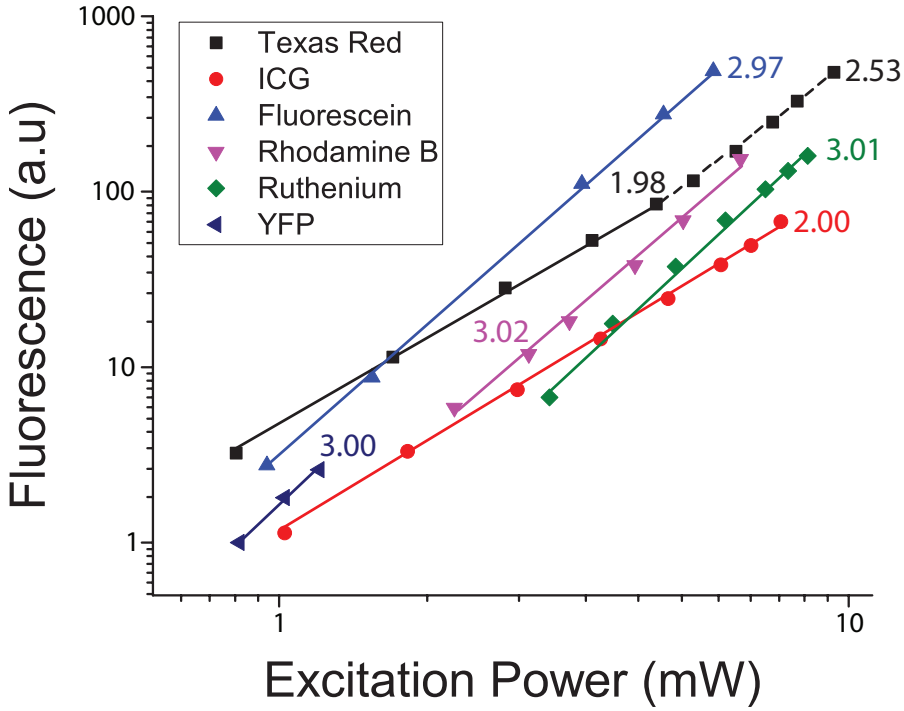


Figure 5.2: Logarithmic power dependence plot for common fluorophores. The slope indicates the  $n$ -photon excitation.

Accurately measuring the two- and three-photon action cross section of a fluorophore is difficult due to the many parameters that must be measured.

The three-photon action cross section,  $\eta\sigma_3$ , is defined as:

$$\eta\sigma_3 = 3\langle F^{(3)}(t) \rangle \frac{(f\tau)^2}{0.51} \frac{1}{\phi C n_o} \frac{8\lambda^3}{28.1(NA)^2 \langle P(t)^3 \rangle}, \quad (5.1)$$

where  $\eta$  is the fluorescence quantum efficiency,  $\sigma_3$  is the three-photon absorption cross section,  $\langle F^{(3)}(t) \rangle$  is the time-averaged fluorescence photon flux,  $\phi$  is the system collection efficiency,  $C$  is the concentration of the fluorophore,  $n_o$  is the refractive index of the sample media, and  $\lambda$  is the excitation wavelength in vacuum. Measuring the system collection efficiency of a system is difficult,

and the nonlinear dependence of the three-photon cross section on numerous parameters makes the measurements very sensitive to any errors. I performed the measurement of the three-photon action cross section of Fluorescein, shown in Figure 5.3, following the methods presented in [22]. The measurement is in good agreement with one previously published value [22]. Future work should aim to measure the action cross sections for all aforementioned fluorescent dyes and proteins as well as other common fluorophores.

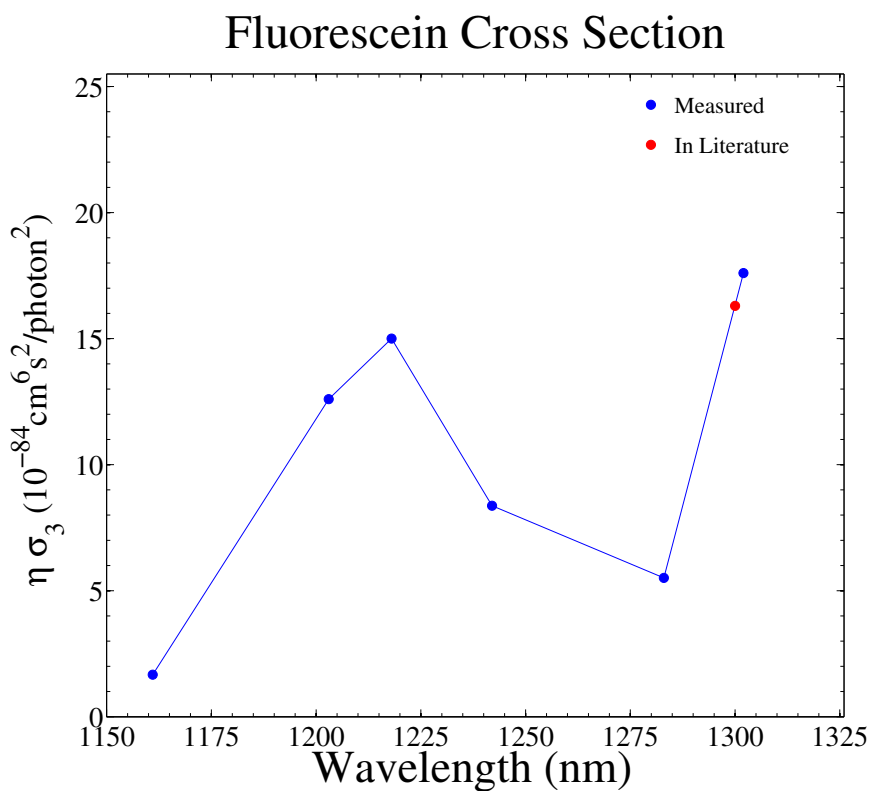


Figure 5.3: The three-photon action cross section for Fluorescein across the OPA excitation wavelengths.

## Chapter 6

### Conclusion

#### Summary

The deep-imaging multiphoton microscopy imaging system described extends the imaging depth of traditional two-photon microscopy to beyond 1 mm. The novelty of the microscope is the tunable long-wavelength, high-pulse-energy light source. I have demonstrated imaging depths of 1,200  $\mu\text{m}$  for vasculature and 1,160  $\mu\text{m}$  for neurons. Based on a theoretical model for the maximum imaging depth of multiphoton microscopy, I estimate the imaging depth of the OPA system could be extended beyond 1,600  $\mu\text{m}$  and identify upgrades to the microscope objective and OPA laser system to realize this depth experimentally. Extending the imaging depth will also require using bright fluorophores with the optimal excitation wavelength. I have demonstrated many common fluorophores undergo 2PE and 3PE across the OPA spectrum, and characterized the brightness of one fluorophore.

#### Future Work

Future work should aim to continue optimizing the OPA laser system and multiphoton microscope optics to further extend imaging depth. A complete characterization of the brightness of common fluorophores at longer

wavelength is necessary. Additionally, dyes that do not clear quickly from the blood stream should be investigated. As the imaging depth increases, the time it takes to complete a 3D stack also increases. Thus, it is imperative to choose dyes that are not cleared from the blood stream quickly, but instead maintain high concentrations throughout the entire imaging session. Fluorescent proteins are a nice solution to the dye-clearing problem, however they face their own issues. One, it is difficult to label vasculature with fluorescent proteins. Two, it can be difficult to control the expression of the fluorescent protein, especially over extended periods of time. One promising route for labeling neurons is with a viral injection, which our lab has used previously. I expect the imaging depth can be extended to 2 mm by using bright fluorophores with two-photon action cross sections near 200 GM and increasing the OPA excitation power reaching the sample surface.

## Bibliography

- [1] Winfried Denk, James H. Strickler, and Watt W. Webb. Two-photon laser scanning fluorescence microscopy. *Science*, 248:73–76, 1990.
- [2] Fritjof Helmchen and Winfried Denk. Deep tissue two-photon microscopy. *Nat. Methods*, 2:932–940, 2005.
- [3] E. Beaurepaire, M. Oheim, and J. Mertz. Ultra-deep two-photon fluorescence excitation in turbid media. *Opt. Comm.*, 188:25–29, 2001.
- [4] Patrick Theer, Mazahir T. Hasan, and Winfried Denk. Two-photon imaging to a depth of 1000  $\mu\text{m}$  in living brains by use of  $\text{Ti}:\text{Al}_2\text{O}_3$  regenerative amplifier. *Opt. Lett.*, 28:1024–1022, 2003.
- [5] Demirhan Kobat, Nicholas G. Horton, and Chris Xu. In vivo two-photon microscopy to 1.6-mm depth in mouse cortex. *J. Biomed. Opt.*, 16:106014–1–106014–4, 2011.
- [6] Nicholas G. Horton, Ke Wang, Demirhan Kobat, Catharine G. Clark, Frank W. Wise, Chris B. Schaffer, and Chris Xu. In vivo three-photon microscopy of subcortical structures within an intact mouse brain. *Nature Photonics*, 7:205–209, 2013.
- [7] David R. Rivera, Christopher M. Brown, Dimitre G. Ouzounov, Ina Pavlova, Demirhan Kobat, Watt W. Webb, and Chris Xu. Compact

and flexible raster scanning multiphoton endoscope capable of imaging unstained tissue. *PNAS*, 108:17598–17603, 2011.

- [8] Supang Khondee and Thomas D. Wang. Progress in molecular imaging in endoscopy and endomicroscopy for cancer imaging. *J. Healthc Eng.*, 4:1–22, 2013.
- [9] Giulio Cerullo and Sandro De Silvestri. Ultrafast optical parametric amplifiers. *Rev. Sci. Instrum.*, 74:1–18, 2003.
- [10] Chris Xu, Jeffrey Guild, Watt W. Webb, and Winfried Denk. Determination of absolute two-photon excitation cross sections by in situ second-order autocorrelation. *Opt. Lett.*, 20:2372–2374, 1995.
- [11] S. M. Shams Kazmi, Anthony J. Salvaggio, Arnold D. Estrada, Michael A. Hemati, Nazariy K. Shaydyuk, Emmanuel Roussakis, Theresa A. Jones, Sergei A. Vinogradov, and Andrew K. Dunn. Three-dimensional mapping of oxygen tension in cortical arterioles before and after occlusion. *Biomed. Opt. Express*, 4:1061 – 1073, 2013.
- [12] Arnold D. Estrada. High-resolution measurement of dissolved oxygen concentration in vivo using two-photon microscopy (doctoral thesis). *Available from UT Austin*, 2011.
- [13] Adrian Negrean and Huibert D. Mansvelder. Optimal lens design and use in laser-scanning microscopy. *Biomed. Opt. Express*, 5:1588–1609, 2014.

- [14] Philbert S. Tsai, Pablo Blinder, Benjamin J. Migliori, Joseph Neev, Yishi Jin, Jeffrey A. Squier, and David Kleinfeld. Plasma-mediated ablation: An optical tool for submicrometer surgery on neuronal and vascular systems. *Curr. Opin. Biotech.*, 20:90–99, 2009.
- [15] Evan P. Perillo, Justin E. McCracken, Daniel C. Fernée, John R. Goldak, Flor A. Medina, David R. Miller, Hsin-Chih Yeh, and Andrew K. Dunn. Deep in vivo two-photon microscopy with a low cost custom built mode-locked 1060 nm fiber laser. *Biomed. Opt. Express*, 7:324–334, 2016.
- [16] Chris Xu and Watt W. Webb. Measurement of two-photon excitation cross sections of molecular fluorophores with data from 690 to 1050 nm. *Opt. Soc. Am. B*, 13:481–491, 1996.
- [17] Chris Xu, Warren Zipfel, Jason B. Shear, Rebecca M. Williams, and Watt W. Webb. Multiphoton fluorescence excitation: New spectral windows for biological nonlinear microscopy. *Proc. Natl. Acad. Sci.*, 93:10763–10768, 1996.
- [18] M. A. Albota, C. Xu, and W. W. Webb. Two-photon fluorescence excitation cross sections of biomolecular probes from 690 to 960 nm. *Appl. Optics*, 37:7352–7356, 1998.
- [19] Nikolay S. Makarov, Mikhail Drobizhev, and Aleksander Rebane. Two-photon absorption standards in the 550-1600 nm excitation wavelength range. *Opt. Express*, 16:4029–4047, 2008.

- [20] Mikhail Drobizhev, Nikolay S. Makarov, Shane E. Tillo, Thomas E. Hughes, and Aleksander Rebane. Two-photon absorption properties of fluorescent proteins. *Nat. Methods*, 8:393–399, 2011.
- [21] Demirhan Kobat, Michael E. Durst, Nozomi Nishimura, Angela W. Wong, Chris B. Schaffer, and Chris Xu. Deep tissue multiphoton microscopy using longer wavelength excitation. *Opt. Express*, 17:13354–13364, 2009.
- [22] Li-Chung Cheng, Nicholas G. Horton, Ke Wang, Shean-Jen Chen, and Chris Xu. Measurements of multiphoton action cross sections for multiphoton microscopy. *Biomed. Opt. Express*, 5:3427–3433, 2014.
- [23] Chun-Yu Lin, Chi-Hsiang Lien, Keng-Chi Cho, Chia-Yuan Chang, Nan-Shan Chang, Paul J. Campagnola, Chen Yuan Dong, and Shean-Jen Chen. Investigation of two-photon excited fluorescence increment via crosslinked bovine serum albumin. *Opt. Express*, 20:13676, 2012.
- [24] Christian J Schrandt, SM Shams Kazmi, Theresa A Jones, and Andrew K Dunn. Chronic monitoring of vascular progression after ischemic stroke using multiexposure speckle imaging and two-photon fluorescence microscopy. *JCBFM*, 35:933–942, 2015.
- [25] N. Nishimura, C. B. Schaffer, B. Friedman, P. D. Lyden, and D. Kleinfeld. Penetrating arterioles are a bottleneck in the perfusion of neocortex. *Proc. Natl. Acad. Sci.*, 104:365–370, 2007.

- [26] Hossmann KA. Pathophysiology and therapy of experimental stroke. *Cell Mol. Neurobiol.*, 26:1057–1083, 2006.
- [27] Timothy H. Murphy and Dale Corbett. Plasticity during stroke recovery: from synapse to behaviour. *Nat. Rev. Neuroscience*, 10:861–872, 2009.
- [28] Steven L. Jacques. Optical properties of biological tissues: a review. *Phys. Med. Biol.*, 58:R37–R61, 2013.